ADVANCED MATERIALS
www.advmat.de

Engineering Mesoscopic 3D Tumor Models with a Self-Organizing Vascularized Matrix

Federica De Lorenzi, Nadja Hansen, Benjamin Theek, Rasika Daware, Alessandro Motta, Saskia Breuel, Ramin Nasehi, Julian Baumeister, Jan Schöneberg, Natalija Stojanović, Saskia von Stillfried, Michael Vogt, Gerhard Müller-Newen, Jochen Maurer, Alexandros Marios Sofias, Twan Lammers, Horst Fischer,* and Fabian Kiessling**

Advanced in vitro systems such as multicellular spheroids and lab-on-a-chip devices have been developed, but often fall short in reproducing the tissue scale and self-organization of human diseases. A bioprinted artificial tumor model is introduced with endothelial and stromal cells self-organizing into perfusable and functional vascular structures. This model uses 3D hydrogel matrices to embed multicellular tumor spheroids, allowing them to grow to mesoscopic scales and to interact with endothelial cells. It is shown that angiogenic multicellular tumor spheroids promote the growth of a vascular network, which in turn further enhances the growth of cocultivated tumor spheroids. The self-developed vascular structure infiltrates the tumor spheroids, forms functional connections with the bioprinted endothelium, and can be perfused by erythrocytes and polystyrene microspheres. Moreover, cancer cells migrate spontaneously from the tumor spheroid through the self-assembled vascular network into the fluid flow. Additionally, tumor type specific characteristics of desmoplasia, angiogenesis, and metastatic propensity are preserved between patient-derived samples and tumors derived from this same material growing in the bioreactors. Overall, this modular approach opens up new avenues for studying tumor pathophysiology and cellular interactions in vitro, providing a platform for advanced drug testing while reducing the need for in vivo experimentation.

1. Introduction

Animal experimentation is essential in biomedical research, but ethical considerations motivate efforts for reducing, replacing, and refining in vivo experiments, in line with the "3R principle".[1] One way to adhere to this principle is to develop advanced, physiologically relevant in vitro models that provide biological readouts with similar predictive power to in vivo tumors.[2]

While 2D in vitro models have provided important insights into basic cancer cell biology,[3] they fall short in reproducing relevant pathophysiological parameters of solid malignancies, such as the tissue mechanical properties and architecture, the heterotypic cell interactions, and the vascular and stromal barriers. These limitations have impelled the development of more complex in vitro models, including 3D in vitro multicellular tumor spheroids (3D MCTS), which are composed of multiple (cancer and

F. De Lorenzi, B. Theek, R. Daware, A. Motta, A. M. Sofias, T. Lammers
Department of Nanomedicine and Theranostics
Institute for Experimental Molecular Imaging (ExMI)
RWTH Aachen University Hospital
52074 Aachen, Germany
E-mail: tlammers@ukaachen.de

F. De Lorenzi, J. Baumeister, A. M. Sofias, T. Lammers
Mildred Scheel School of Oncology (MSSO)
Center for Integrated Oncology Aachen Bonn Cologne Düsseldorf (CIO^{ABCD})
RWTH Aachen University Hospital
52074 Aachen, Germany

N. Hansen, R. Nasehi, J. Schöneberg, N. Stojanović, H. Fischer
Department of Dental Materials and Biomaterials Research (ZWBF)
RWTH Aachen University Hospital
52074 Aachen, Germany
E-mail: hfischer@ukaachen.de

S. Breuel, J. Maurer
Department of Gynecology and Obstetrics
RWTH Aachen University Hospital
52074 Aachen, Germany

The ORCID identification number(s) for the author(s) of this article can be found under https://doi.org/10.1002/adma.202303196

DOI: 10.1002/adma.202303196

stromal) cell types in 3D spherical patterns. These 3D models more accurately replicate the spatial complexity of solid malignancies and display greater molecular and histological similarities to solid malignancies in vivo, compared to cultivation conditions in 2D monolayers.[4–6] Additionally, 3D MCTS can be introduced in extracellular matrix (ECM)-mimicking hydrogels. The possibility to fine-tune the properties of ECM mimics allows researchers to investigate how certain ECM features, such as stiffness, relaxation behavior, and crosslinking, contribute to various pathophysiological changes, e.g., the epithelial-to-mesenchymal transition (EMT) of cancer cells, i.e., the formation of motile mesenchymal-like clones from nonmotile epithelial cells).[7,8] Nevertheless, most of the existing 3D models lack functional vascularization. Thus, angiogenesis, one important hallmark of cancer, is not properly reflected and long-term cultivation is challenging due to insufficient diffusion of nutrients and oxygen.[4] The lack of fluidity also challenges studying the interaction of cancer cells with functional vessels, i.e., the important step of tumor cell invasion representing the transition to a metastatic phenotype. Furthermore, the tumor crosstalk with circulating blood and immune cells as well as drug delivery over vascular and stromal barriers, including processes related to the enhanced permeability and retention effect, can hardly be investigated.[9]

Advances in the fields of microfabrication and microfluidics have greatly contributed to the development of vascularized multicellular models that replicate the functional units of human organs.[10,11] The most popular approaches utilize polydimethylsiloxane (PDMS) chips with parallel microchannels, either containing cell-laden hydrogels or flowing growth medium. In such setups, the flow of growth medium is usually induced by a hydrostatic pressure gradient between two medium reservoirs, resulting in a relatively slow flow rate.[12,13] The formation of a capillary bed is typically achieved by leveraging the ability of endothelial cells (EC) to self-assemble and form micro-vascular networks when grown in 3D hydrogel-based matrices. This enables the investigation of the impact of shear stress and flow velocity on vascular sprout formation and elongation.[14–17] Moreover, PDMS chips with cancer, EC and stromal cells have been used for evaluating anti-angiogenic and cytostatic drugs.[18,19] Recently, PDMS chips were functionalized with a central well to house a multicellular spheroid composed of EC, stromal, and cancer cells.[20] The study highlighted the challenges of mimicking successful intratumoral angiogenesis in vitro, as it was only achieved with one out of four cancer cell lines tested, and only upon the use of a triculture spheroid.[20] 3D tumor spheroids were also embedded in a perfusable microvascular network grown in PDMS chips to study the dynamics of drug transport in vitro.[21] Factors that have contributed to the popularity and success of PDMS chips include low material consumption, thus enabling high throughput experiments. In addition, PDMS chips are optically transparent, and the single-plane organization of cells near the device's surface facilitates single-cell tracking and the imaging of cell–cell interactions.[13] However, the restricted inner thickness of PDMS chips, which is typically less than 500 μm hinders the growth of tumor spheroids to the millimeter scale. This limitation is critical as the "angiogenic switch" is hypothesized to occur in vivo in certain solid malignancies, like colon carcinoma, only after the tumors exceed diameters of 1–2 mm.[22,23] Additionally, in PDMS chips, the rectangular geometry of the channels in which EC are patterned prevents the faithful replication of physiological flow dynamics.

Several alternatives have already been explored to fabricate channel networks embedded within ECM-mimicking hydrogel matrices. These methods either involve direct bioprinting of vessel-like structures, or indirect printing of 3D channel templates using soluble fugitive bioinks, followed by casting of the ECM hydrogel and EC lining.[24–27] Compared to PDMS chips, the bioprinting techniques have facilitated a shift in the size of vascularized tissue from the micro- to the mesoscopic scale. In addition, bioprinted constructs have demonstrated durability under fluid flow conditions for up to four weeks.[25] Bioprinted vessel-like structures have been utilized to sustain the growth of patient-derived cancer and stromal cells.[28] However, these approaches do not fully replicate natural anastomosis or the formation of a tumor vasculature comprising vessels with varying calibers. The use of porous hydrogels with well-defined geometries ranging from millimeters to micrometers can partially address these limitations.[29,30] In this context, anastomoses between vessels of different calibers are induced by lining EC within hydrogels that feature prefabricated structures. However, also this method does not reflect the tissue-specific vascular features that develop during natural and pathophysiological angiogenesis.

We previously created a multilayered artificial vessel using 3D bioprinting and a combination of three cell types (EC, smooth muscle cells, and fibroblasts), replicating the tunica intima, media, and adventitia.[27] The dynamic cultivation of our vessel-like structure resulted in a mature, physiological barrier, comparable to in vivo vessels.[27] This structure is used in the present study

J. Baumeister
Department of Hematology
Oncology
Hemostaseology and Stem Cell Transplantation
RWTH Aachen University Hospital
52074 Aachen, Germany

S. von Stillfried
Institute of Pathology
RWTH Aachen University Hospital
52074 Aachen, Germany

M. Vogt
Interdisciplinary Center for Clinical Research (IZKF)
RWTH Aachen University Hospital
52074 Aachen, Germany

G. Müller-Newen
Institute of Biochemistry and Molecular Biology
RWTH Aachen University Hospital
52074 Aachen, Germany

A. M. Sofias
Norwegian University of Science and Technology (NTNU)
Department of Circulation and Medical Imaging
Faculty of Medicine and Health Sciences
Trondheim 7491, Norway

F. Kiessling
Institute for Experimental Molecular Imaging (ExMI)
RWTH Aachen University Hospital
52074 Aachen, Germany
E-mail: fkiessling@ukaachen.de

F. Kiessling
Fraunhofer Institute for Digital Medicine MEVIS
28359 Bremen, Germany

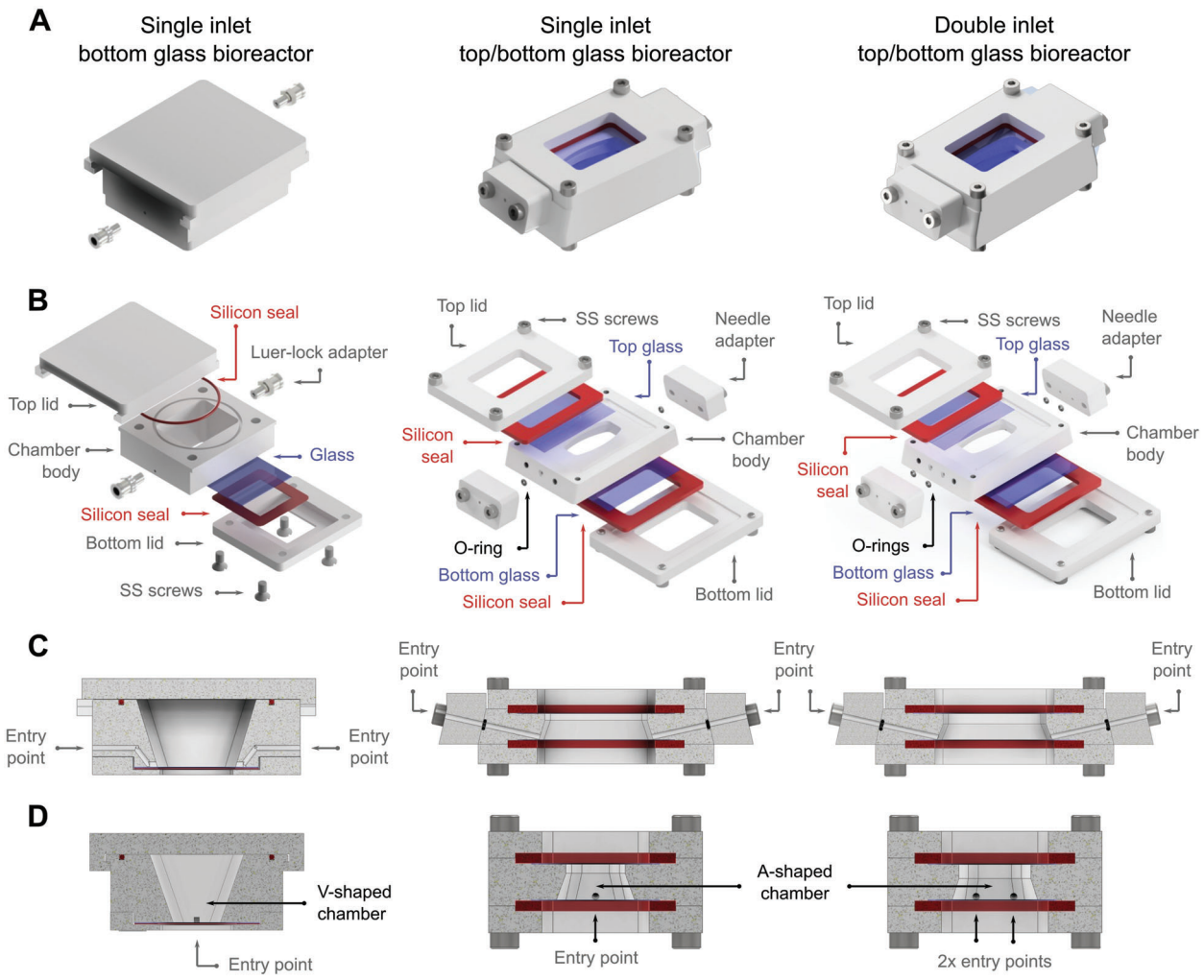

Figure 1. Development of bioreactors for supporting and monitoring physiological tumor growth. A) 3D rendering of assembled bioreactors. B) Exploded schematic exemplifying the design and components of the three bioreactor types. Bioreactors were designed with single or double inlets/outlets, a lid, rubber silicon seals, and with optical windows only at the bottom or on both sides. Stainless steel (SS) screws were used to tightly close the bioreactor when assembled, ensuring a leak-proof seal. For connecting the bioreactors to fluid flow, the chamber's body was functionalized with metal Luer-lock adapters or needle adapters. C,D) Sagittal and axial views of bioreactors exemplify the unique features of the bioprinting chambers, including the chamber shape (V-shaped or A-shaped), the thickness of the silicon seals (which is important for ensuring appropriate sealing), and the design of the entrance region.

to support the progression of artificial tumors. By combining direct bioprinting and the self-organization of EC, structured microvascular networks were formed in a 3D hydrogel matrix. The growth of a tumor spheroid to the mesoscopic scale, its transition to a metastatic phenotype, and the interaction of cancer cells with the vascularized ECM, were monitored over the course of weeks, and the system was optimized to mimic tumor angiogenesis. In addition, the system was tested for its functionality, and it was used to cultivate patient-derived cancer cells, demonstrating its ability to capture the phenotypic heterogeneity of human malignancies compared to engrafted tumor models. Our 3D bioprinted tumor model has the potential to provide an accurate simulation of various cancer stages and types, and it is a valuable tool for preclinical research and drug development, which can ultimately contribute to the refinement and potentially reduction of animal experimentation.

2. Results and Discussion

2.1. Development and Evolution of Custom-Made 3D-Printed Bioreactors

Three types of devices were conceptualized and designed for supporting the growth of a biologically active system, on the basis of previously developed custom-built bioreactors[27] (**Figure 1**A). Polyether-ether ketone (PEEK) was chosen as the target material, because of its favorable properties, including sterilization resistance at high temperature, biological and imaging compatibility (including CT, MRI, and US), as well as long-term durability.[31] Unlike PDMS chips, PEEK does not adsorb hydrophobic substances (e.g., growth factors), thereby preserving the integrity of cell–cell signaling pathways mediated by secretion of such substances.

Each custom-built bioreactor was specifically designed to allow cultivation under fluid flow conditions. Silicon seals were used to ensure both leakproofness and airtightness (Figure 1B). The bioreactors were outfitted with a lid, facilitating the harvesting and processing of cellular material for histology[27] (Figure 1B). In addition, for enabling real-time monitoring of cell organization, particularly when fluorescent-tagged cells were used (i.e., GFP-HUVEC), bioreactors were functionalized with an optical window that is compatible with fluorescence and multiphoton microscopy (Figure 1B).

The first bioreactor type, equipped with a glass bottom and a lid (Figure 1A,B) served to optimize the functionality and reproducibility of the model. This device featured Luer-lock connectors to gas-permeable silicon tubes for dynamic cultivation. However, real-time monitoring of structural defects was not possible in this bioreactor due to the absence of a transparent window on the body chamber's top. Such defects included medium accumulation at the entrance region of the bioreactor or on the hydrogel, as well as hydrogel holes caused by cancer cells degrading the matrix faster than stromal cells could deposit new ECM. As a result, the top lid needed to be opened for monitoring the bioreactors for potential defects.

The second and third type bioreactors were developed to enable continuous observation of the hydrogel's response to the fluid flow and the activity of the resident cells. They were outfitted with coverslips on both, the top and the bottom of the bioreactor's body. The metal Luer-lock adapters of type one bioreactors were replaced by PEEK adapters equipped with O-ring sealing and needles, freeing up space for up to two inlets and outlets (Figure 1B,C). The use of needles at the entrance region further ensured a smoother flow of medium through the entire body of the bioreactor, eliminating corners where air bubbles could accumulate (Figure 1B,C). Additionally, the printing area was enlarged, while the chamber height was reduced. These modifications allowed for printing more complex structures, while reducing the hydrogel amounts and weight, thus improving the overall vascular network stability. Other modifications were made, including changing the chamber orientation, from a V-shaped design to an A-shape (bioreactor cross-section in Figure 1D), and changing the chamber shape from a rectangular to an oval contour along the longitudinal direction for preventing the hydrogel detachments from the coverslip or wall under hydrostatic pressure changes (Figure 1B). Overall, the development of these three bioreactors facilitated the printing of simple to complex vascular structures, ensuring long-term stability under fluid flow irrespective of the complexity of the printed structures. Although all three bioreactors could be used for our experiments, the final design resulted in the best performance in terms of robustness, and handling.

2.2. Bioprinting of Vascular Structures with Different Fluid Flow Dynamics

The next step in the development of functional bioreactors involved the bioprinting of different vascular structures serving as feeding vessels for the tumoroids positioned in the center of the bioreactors. To achieve a native-like vascular architecture, characterized by branching and curvature, and to replicate fluid flow properties across distinct branches, we utilized 3D bioprinting to create three different configurations of feeding vessels (**Figure 2**). The different designs took the form of (i) a single-branched oval channel, (ii) a double hexagon-shaped channel with secondary branches, and (iii) two simple parallel straight channels (Figure 2A).

High-resolution CT scanning was applied to provide accurate measurements of the bioprinted structures (Figure 2A). The first 3D bioprinted structure was a single gelatin strand of 0.77 ± 0.05 mm in diameter that branched, creating an oval-shaped space measuring 2.5 mm along the minor axis and 4.6 mm along the major axis, with a total length of 16 mm. The second design was more complex, featuring a double hexagon-shaped channel with secondary S-shaped branches of 0.54 mm ± 0.02 in diameter. To construct this design, we printed a single gelatin strand that branched into two sequential hexagonal-shaped spaces of 6 mm. Within these spaces, we printed two smaller channels in an S-shape. The entire length of this structure was 28 mm. Finally, for the third design, we bioprinted two parallel gelatin strands measuring 0.93 ± 0.14 and 28 mm in total length, with an average distance of 6.5 mm between the channel walls. By using computational modeling, we estimated the fluid flow dynamics, including flow velocity and wall shear stress across the different vascular structure designs (Figure 2B,C; Figure S1, Supporting Information). By setting the volumetric flow rate to 0.1 mL min^{-1} in the single-branched oval channel, we simulated maximum flow velocities of 4 mm^{-1} s at the entrance region of the bioreactor. This may account for the occasional structural issues observed in this particular area during the use of the first type of bioreactors. We further simulated a uniform velocity and shear stress within the parallel vascular structures. Conversely, the more complex structure, which included primary and secondary branches, showed a decrease in both velocity and shear stress in areas distanced from the primary channel (Figure 2B,C; Figure S1, Supporting Information). Complementing our simulations, we utilized high-resolution CT measurements to confirm the post-printing shape and size of the channels, as well as their stability after 24 h of perfusion. These assessments showed an increase in circularity nearing unity, and diameters of 1.27 ± 0.15 mm for the single-branched oval shaped channel, 1.30 ± 0.45 mm for the complex one, and 1.18 ± 0.12 mm for the parallel straight channels (Figure 2D,E). The data substantiate that the bioprinted structures do not collapse under fluid flow conditions. The increase in their size over time is likely related to a combination of hydrogel contraction and pressure from circulating medium within the bioreactor.[32]

2.3. Development of Bioreactors Containing Mesoscopic Vascularized Cancer Organoids

While Matrigel is widely used as an extracellular matrix (ECM) analog, there are concerns about transmission of animal pathogens and large batch-to-batch variability, (which can induce a high heterogeneity in organoid composition and growth). These have led to a growing interest in alternative natural and synthetic polymer scaffolds.[33] Natural hydrogels, such as collagen and fibrin, are often utilized due to their high density of cell-binding sites, ease of remodeling by resident cells, and off-the-shelf

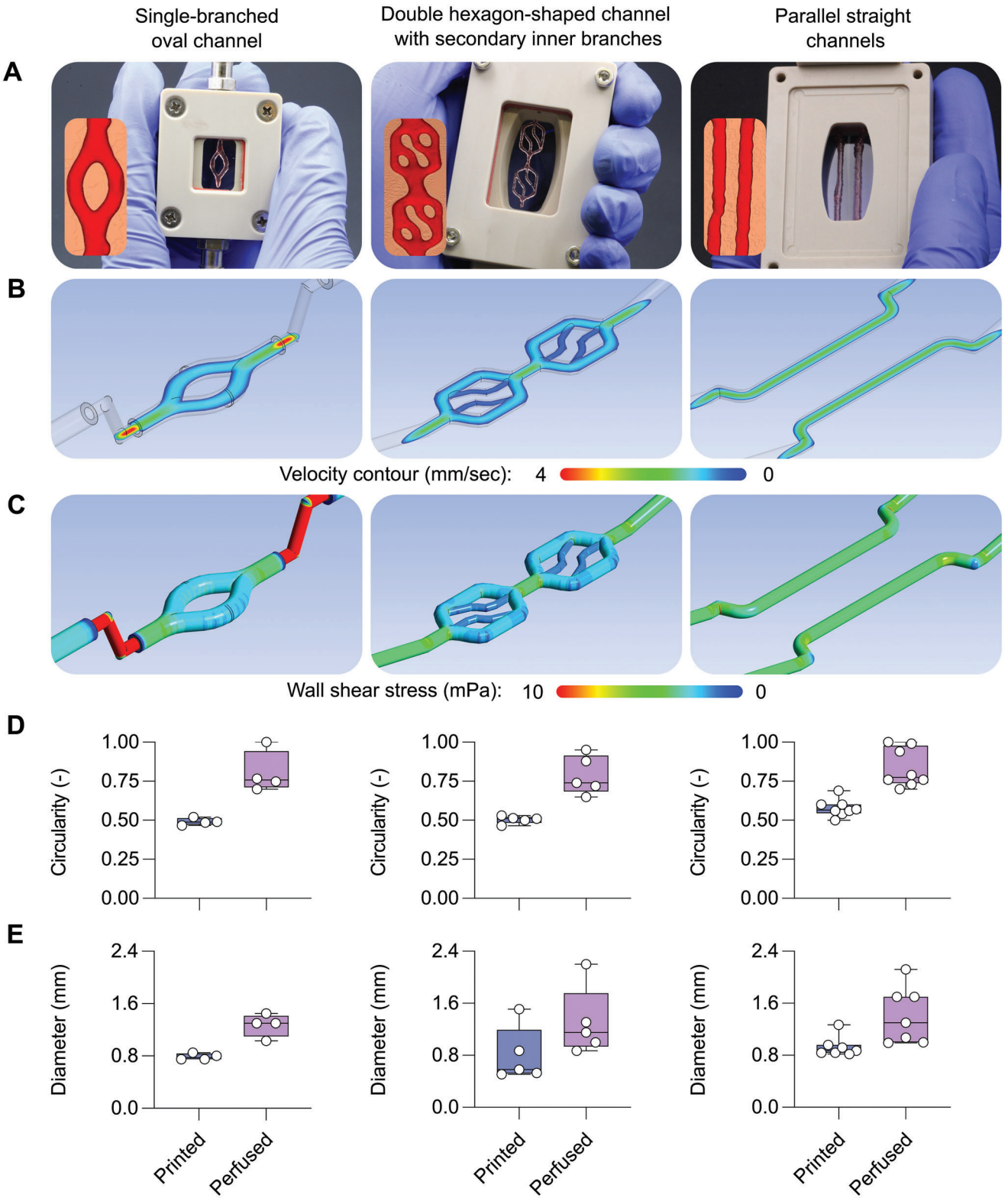

Figure 2. Evolution of printed vascular structures design. A) Photographs and 3D-rendered high-resolution CT images of the three different vascular-like structures inside the bioreactors. B) Contour plots of flow velocity within the cross section of the printed vessel were obtained from numerical simulation of fluid flow using Ansys CFX. The volumetric flow rate in channels was set to 0.1 mL min^{-1}, which is the flow rate used in actual experiments. C) Computation of wall shear stresses emphasizes differing values in branched versus straight channels. D,E) The bioprinted vascular structures were scanned with high-resolution CT directly after printing, and after 1 d of dynamic cultivation to assess diameter and circularity, and to investigate stability under conditions of fluid flow. The measurements indicate that channels remained round and did not collapse in response to fluid flow.

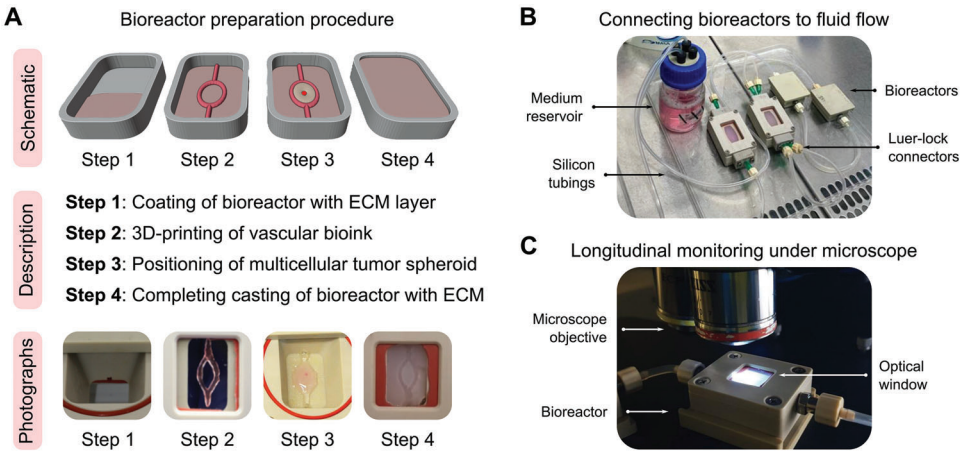

Figure 3. Workflow for creating perfused mesoscopic artificial tumors. A) The process started with the placement of an ECM layer at the bottom of the bioreactor to increase the adherence of the hydrogel to the glass slide (step 1). Vascular strands (gelatin mixed with EC) were bioprinted to form an oval space in which a tumor spheroid in ECM containing either fibroblasts or fibroblasts and EC was positioned (steps 2 and 3). Finally, the bioreactor was filled with ECM (step 4). B) Gelatin was removed and sterile perfusion was applied using a peristaltic pump in a recirculating flow loop. C) EC organization and tumor spheroid growth were monitored by fluorescence microscopy.

availability.[34] Collagen hydrogels can be formed by adjusting the pH and temperature of extracted collagen solutions.[35] However, since collagen lacks mechanical strength, it is often combined with fibrin gel to produce biofunctional blends with optimal mechanical properties.[27,34–36] A polymerized fibrin gel similar to a physiological clot can be easily synthesized in vitro by mixing fibrinogen with thrombin and calcium chloride ($CaCl_2$).[35,36] For the development of our model, a naturally-derived fibrin-collagen hydrogel blend was used as ECM substitute. Transglutaminase, antifibrinolytics tranexamic acid, and aprotinin were added to improve the mechanical stability of the hydrogel for long-time cultivation under fluid flow and to reduce degradation by resident cells[25,27,37] (Figure S2, Supporting Information). This blend was applied to coat our PEEK bioreactors to improve hydrogel adherence to the glass bottom (**Figure 3**A). Next, a vascular-like structure was 3D-bioprinted directly inside the bioreactors using a vascular bioink of gelatin mixed with EC (Figure 3A). This bioink served as fugitive material.

A multicellular spheroid of cancer and stromal cells was harvested, resuspended in the fibrin-collagen hydrogel blend and positioned in the space comprised by the branched vascular structures (Figure 3A). To resemble the composition of the tumor stroma, the hydrogel blend surrounding the tumor spheroid was supplemented with fibroblasts or fibroblasts and EC (Figure 3A). After solidification of the fibrin-collagen mixture at room temperature, bioreactors were incubated at 37 °C in rotation to allow homogenous attachment of EC to the lumens' walls while the gelatin ink became liquid. The fugitive material was then removed with warm PBS leaving endothelialized hollow cores. Bioreactors were connected to a peristaltic pump in a recirculating fluid loop and dynamically cultivated for up to three weeks (Figure 3B). The dynamic fluid flow regimen was applied at a flow speed of 0.1 mL min^{-1}, imparting wall shear stress values of ≈0.01–0.03 dyn cm^{-2}. The medium reservoir consistent of a mix of growth media of the cell types used for the model, and half of its content was changed every second day, following previously established protocols.[23] The formation of a continuous EC monolayer, its maintenance over the course of weeks, and its capacity to restrain the diffusion of large molecules were found to be consistent with our previously reported work.[27] Importantly for maintaining neutral hydrostatic pressure values within the bioreactor, the milliliters of medium inside the flask reservoir were set to match the height of the fluid flow inside the bioreactors. The processes of vascular network development, tumor spheroid growth, and flow dynamics were longitudinally monitored via fluorescence microscopy (Figure 3C).

2.4. The Synergistic Crosstalk between Cancer and Endothelial Cells Enables the Formation of Mesoscopic Vascularized Tumors

For the establishment of the model, we made use of the A431 human squamous carcinoma cell line, which is known for its high secretion of VEGF and prominent angiogenic phenotype when engrafted in animals.[38] These characteristics are in line with histological observations of human surgical specimens of squamous carcinomas that also display a high vascularization (Figure S3, Supporting Information). Round and compact 3D MCTS of A431 cancer cells and fibroblasts were formed by means of hanging-drop technique and their biofunctionality (including proliferation, collagen deposition and formation of hypoxic core) evaluated histologically up to 15 d (Figure S4, Supporting Information). Upon reaching a size of 300 up to 500 µm in diameter, A431 tumor spheroids were harvested and positioned in the bioreactor together with ECM-laden stromal cells (**Figure 4**A–C; Figure S4, Supporting Information).

A first aim was to investigate whether the presence of cancer cells influences the formation of a vascular network in the space comprised by the bioprinted vascular strands. To this end, bioreactors were cast with or without the addition of an A431 tumor spheroid, while the initial concentration of EC and stromal cells was kept constant (Figure 4C,D). After one week of dynamic cultivation, a structured microvascular network developed (Figure 4C). The area of this self-assembled capillary

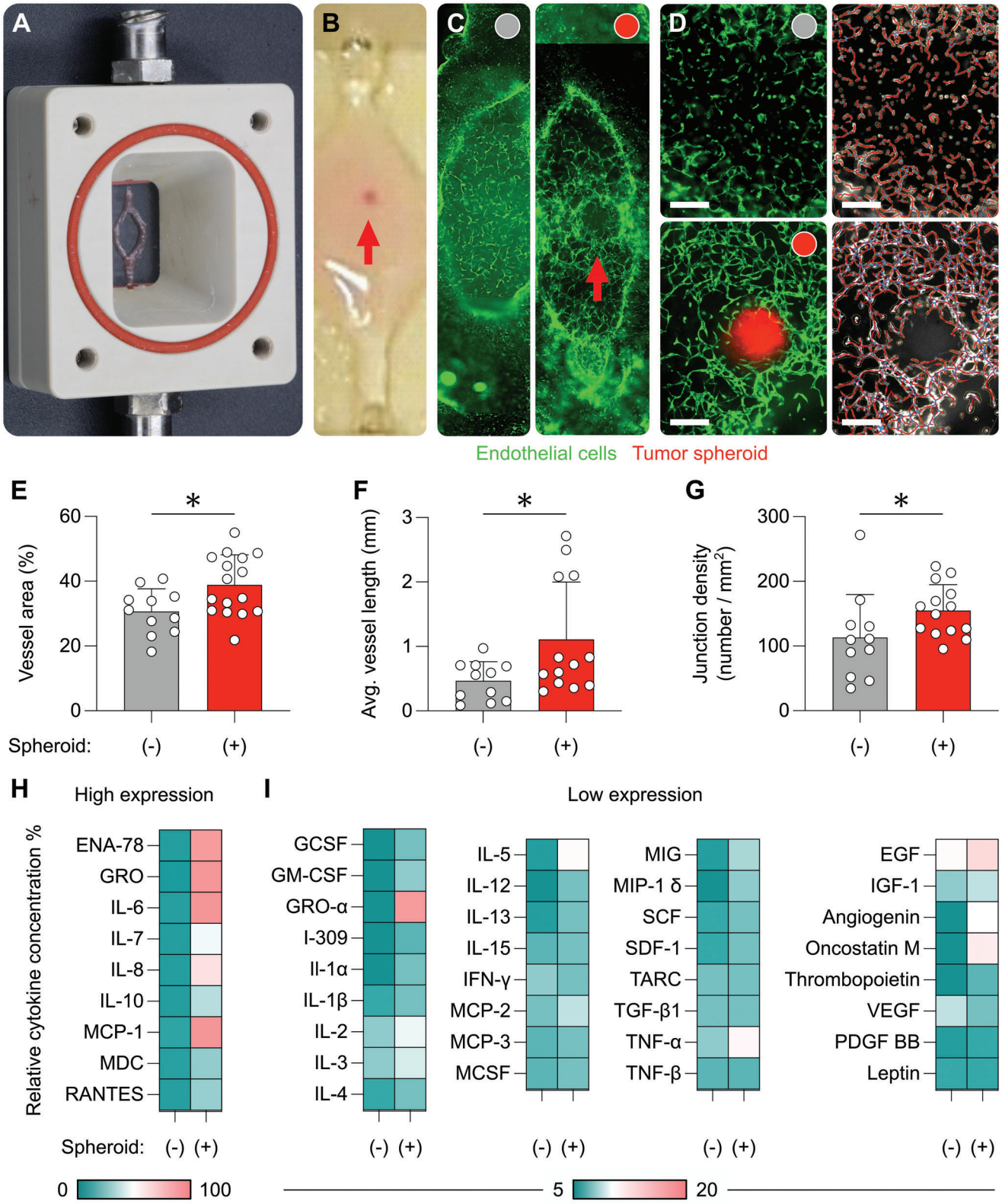

Figure 4. The presence of tumor spheroids enhances vascularization of ECM hydrogel substitutes. A,B) Bright field images display a single-inlet glass bottom bioreactor where branched gelatin strands are 3D-bioprinted to create an oval-shaped space. In the displayed example, a fibrinogen-collagen hydrogel blend containing endothelial cells (GFP-HUVEC), stromal cells (fibroblasts and mesenchymal stem cells), and a tumor spheroid (DiD-labelled A431, human skin squamous cell carcinoma) was cast. The position of the tumor spheroid within the hydrogel blend is indicated by the red arrow. C,D) After seven days of dynamic cultivation, fluorescence microscopy images show a denser and more ramified vascular network between the two

network was larger (Figure 4E) and contained longer (Figure 4F) as well as more ramified vessels (Figure 4G) in presence of angiogenic A431 tumor spheroids, as compared to the control condition (no tumor spheroid was embedded in the hydrogel matrix). Additionally, the medium collected from bioreactors with tumor spheroids upon one week of cultivation was strongly enriched in cytokines and chemokines. Among those are GRO (CXCLs), ENA-78 (CXCL5), IL6, IL7, IL8, MCP-1 (CCL2), and RANTES, which are known to be critically involved in inflammation, immune cell recruitment, and angiogenesis (Figure 4H,I).

Subsequently, the impact of the capillary vascular network on tumor spheroid growth was investigated. To examine this, A431 tumor spheroids were inserted into the bioreactors together with either EC and stromal cells, or stromal cells only in the surrounding ECM-mimicking hydrogel (**Figure 5**A(i–iv)). The longitudinal assessment over 14 days of dynamic cultivation displayed the formation of a well-organized vascular network at the mesoscopic level, only in the presence of EC (Figure 5A(ii,iv)). Furthermore, after 14 d of dynamic cultivation, the average size of tumor spheroids in the presence of both EC and fibroblasts increased significantly more than in bioreactors containing only fibroblasts in the surrounding hydrogel (1.67 ± 0.72 mm^2 vs 0.63 ± 0.19 mm^2, respectively) (Figure 5B). The latter observation highlights the known dependence of tumor progression on angiogenesis.[22]

To rule out that in absence of a vascular network the cells are deteriorating over time, a quantitative analysis of the whole bioreactor content was performed using flow cytometry. Excellent cell viability was found for both configurations (Figure 5C). Moreover, given that the configuration with EC and fibroblasts is biologically more relevant, a more extensive investigation regarding cell viability was conducted. Dead cells were excluded from the analysis via the 7AAD live/dead marker. After 7, 14, and 21 d of dynamic cultivation, cell viabilities of 92%, 91%, and 85% were found, respectively (Figure 5D). Finally, in order to assess changes in the cell composition over time, flow cytometry was employed to differentiate between GFP-positive EC, RFP-positive fibroblasts, and DiD-labelled cancer cells. The analysis showed a progressive increase in the fraction of cancer cells (i.e., the most proliferative population), but also an excellent preservation of the other two cell populations for the full course of the experiment (Figure 5E).

2.5. Refined Bioprinted Vascular Structures Trigger Vascular Sprouting

Endothelial cells respond to both biochemical and mechanical stimuli, which can influence their angiogenic potential and their capacity to form sprouts.[40,41] In our study, we set to mimic the sprouting process of EC from the 3D bioprinted vessel towards inner sections of the hydrogel matrix. For this purpose, we used bioreactors with bioprinted vascular structures and fibroblasts and tumor spheroids in the space formed by the bioprinted vascular strands. We initially hypothesized that modifying the tumors' position relative to the blood vessel could impact the formation of meaningful gradients of angiogenic factors, oxygen, and pH within the construct, which are known triggers for sprouting angiogenesis.[22] To this end, we adjusted the tumors' position relative to the bioprinted vascular-like structure. However, moving the tumor spheroids closer to the feeding vessel did not improve the formation of EC sprouts.

Subsequently, we reduced the concentration of fibrinogen and collagen. Our hypothesis was that a relatively high hydrogel concentration may hinder EC from sprouting or it may adsorb the relevant pro-angiogenic growth factors secreted by cancer and stromal cells, limiting their diffusion to target EC. The hypothesis was formulated from existing literature, which has reported that organ-on-a-chip models, designed to simulate angiogenesis, typically utilize very low concentrations of ECM components (around 2.5 mg mL^{-1} of fibrinogen and 0.2 mg mL^{-1} of collagen, which are approx. four times lower than the final hydrogel concentrations we used in our experiments, see extended materials and methods section in the Supporting Information).[14,15,20] In addition, previous research demonstrated a decrease in the formation of vascular networks in both the length and diameter of EC segments with increasing fibrinogen concentrations.[12,42] In our experimental set-up, low hydrogel concentrations resulted in decreased hydrogel water-retaining capacity, reduced mechanical stability during dynamic cultivation, and EC regression after one week of dynamic cultivation (Figure S2B, Supporting Information). Therefore, low hydrogel concentrations were not considered in our final setup.

Finally, we applied our complex vascular design, consisting of sequential hexagon-shaped channels and two small S-shaped inner branches (Figures 2A and **6**). This aimed to induce variations in lumen size, flow velocity, and wall shear stress. We positioned tumor spheroids among the S-shaped gelatin strands, and observed an extension of vascular sprouts from the S-shaped smaller branches. Mathematical flow modeling revealed that these branches corresponded to regions with reduced values of wall shear stress (Figure 2C). The sprouts formed and elongated towards the interior of the ECM and towards the tumor spheroids, measuring 200–500 μm in length. By day 14, the sprouts were perfused with 10 μm beads and proved to be functional (Figure 6B,C). The average flow velocity in newly formed, elongated vascular sprouts was of 0.22 ± 0.12 mm^{-1} s. Most importantly, the measured velocity of microbeads in different sections of the structure was in concordance with the simulated flow velocity, strengthening the predictive power of our mathematical modeling (comparison between Figure 2B and Figure 6C).

Our modified bioprinted vascular structures in the double capillary bed provided more favorable conditions for the sprouting of EC, resulting in the successful establishment of a functional vascular network. These findings are consistent with recently

branched feeding vessels in the presence of tumor spheroids. Scale bar = 200 μm. E–G) Image analysis revealed that upon seeding the same initial number of EC, the capillary bed was significantly denser and composed of longer and more branched tubular structures in the presence versus absence of a tumor spheroid. H,I) Cytokine concentration % in the culture medium of bioreactors containing A431 spheroids after one week of cultivation versus fresh culture medium. Data in (E)–(G) are displayed as means ± SD of $n = 7$–15 replicates (i.e., bioreactors) across $n = 3$–5 independent experiments. Images in (D) were analyzed with AngioTool software.[39] Statistical significance was assessed via a Mann–Whitney test; $^*P < 0.05$.

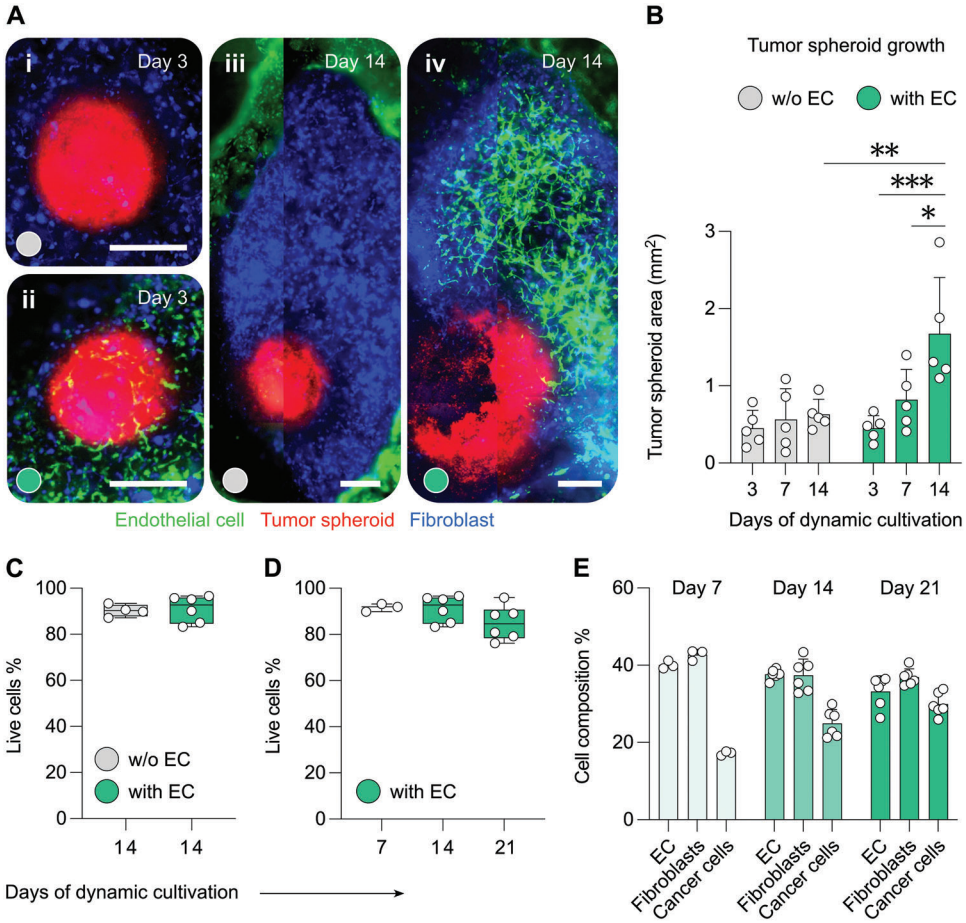

Figure 5. Vascular networks and stroma contribute to the growth of tumor spheroids. A) Longitudinal fluorescence microscopy imaging showing the growth of A431 tumor spheroids (DiD-labeled; in red) in the presence of EC (GFP-expressing HUVEC; in green) and stromal cells (RFP-expressing fibroblasts; blue) over 3 and 14 d of dynamic cultivation. Among the two examined conditions (i.e., only fibroblasts (i,iii), or fibroblasts and EC (ii,iv) at day 3 and 14), the sizes of the spheroids increased significantly more in the presence of EC. Interestingly, central necrosis was also identified in the larger spheroids (iv; dark region in the spheroid), mirroring the in vivo situation. Scale bar = 500 µm. B) Quantitative analysis of spheroid sizes in absence (gray) or presence (green) of EC. C) Percentage of live cells in bioreactors in absence (gray) or presence (green) of EC after 14 d of dynamic cultivation. D) Percentage of live cells in bioreactors in presence of EC after 7, 14, and 21 d of dynamic cultivation. E) The cellular composition in the bioreactors after 7, 14, and 21 d of dynamic cultivation was assessed by flow cytometry, showing an increase in the fraction of cancer cells, as well as the preservation of the endothelial and stromal cell populations. Data in B are displayed as mean ± SD of $n = 5$ bioreactors across $n = 6$ different independent experiments. Data in (C)–(E) are described as mean ± SD of $n = 3$–6 bioreactors across $n = 4$ different independent experiments. Statistical significance in (B) was assessed by a two-way Anova followed by Tukey's test for multiple comparisons; $^*P < 0.05$, $^{**}P < 0.01$, $^{***}P < 0.001$, and $^{****}P < 0.0001$.

published data demonstrating a higher number of vascular sprouts to occur at locations of low shear stress in self-organized capillary networks in PDMS chips.[43] These findings also demonstrate the potential of our system for modeling complex events in cancer biology in vitro at the mesoscopic scale.

2.6. The Self-Assembled Vasculature Infiltrates the Tumor Spheroid and is Functional

A significant challenge in engineering vascularized tissues in vitro is the replication of vascular functionality. The formation of functional blood vessels is essential for ensuring the nutrient and oxygen supply to cells and for studying the dynamics of drug delivery. While the functionality of vascular structures and the endothelium's ability to restrict the diffusion of large molecules have been confirmed in 3D bioprinted structures[25,27,29] and self-organized vascular networks at submillimeter scale,[18–21,44] as well as in case of EC patterned in porous hydrogel matrices,[30,45] to the best of our knowledge, the functionality of a self-organizing vascular network at the mesoscopic scale has yet to be demonstrated.

To validate the functionality of our self-evolving vascularized matrix, we cast bioreactors with tumor spheroids surrounded by EC and stromal cells and cultivated them dynamically for up to three weeks. In-depth analysis revealed that the self-assembled capillary network had infiltrated the tumor mass, sprouting into the first layers of the tumor spheroid (**Figure 7**A). Moreover, upon observing the capillary network using multi-photon microscopy, we discovered that it possessed open lumens, highlighting its potential to transport macromolecules (Figure 7B).

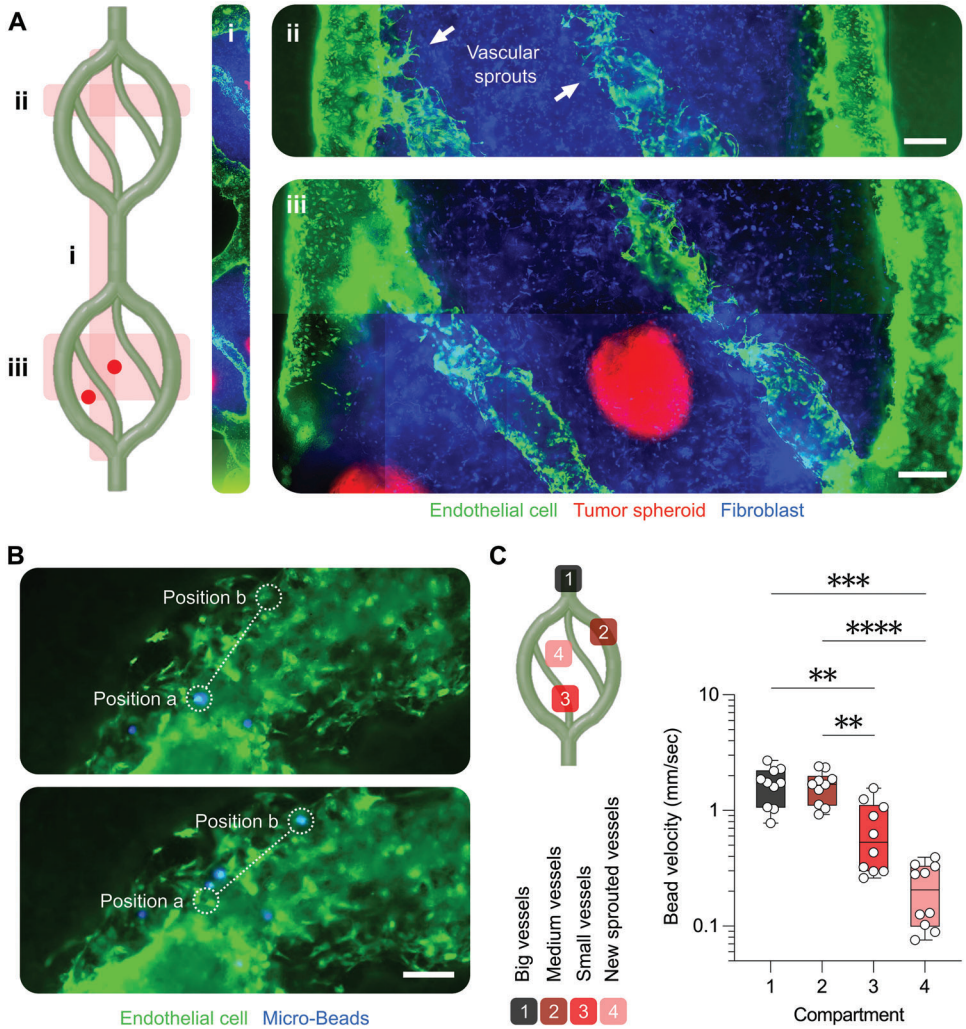

Figure 6. Inducing tumor angiogenesis: A) The schematic exemplifies the design of the bioprinted vascular structure (light green) and the positioning of tumor spheroids (red). The vascular structure comprises two big, sequential hexagon-shaped channels and two small S-shaped inner branches. Fluorescence microscopy images exemplify the arrangement of endothelial cells (GFP-expressing HUVEC, in green) and tumor spheroids (DiD-labelled A431, in red) along the major axis of the construct (I). At day 14 of dynamic cultivation, an elongation of vascular sprouts was observed, which extended towards the interior of the ECM (ii) and towards the tumor spheroids (iii). B) The elongated vascular sprouts were perfusable with 10 µm large beads (blue). Their change in position in two consecutive images illustrates their movement through the newly formed vessel. Scale bar in A-(i) = 200 µm and in A-(ii),(iii) = 500 µm. Scale bar in (B) = 200 µm. C) The flowing beads were analyzed to quantify velocity in different sections of the vascular structures. Data are displayed as velocity values of $n = 10$ individual beads flowing in 4 different vascular sections. Statistical significance was assessed by a Welch ANOVA test with Dunnett's multiple comparisons test; $^{*}P < 0.05$, $^{**}P < 0.01$, $^{***}P < 0.001$, and $^{****}P < 0.0001$.

To take it a step forward, we perfused the system with red blood cells (RBC) after one week of dynamic cultivation. The RBC were introduced in the recirculating flow loop and the bioreactors were observed for up to 24 h by means of fluorescence microscopy. In this setting, RBC appeared black due to light absorbance by hemoglobin. Our results demonstrate that the self-assembled network anastomosed with the bioprinted endothelium and that functional connections were established between two structures (Figure 7C). Most importantly, by focusing on the areas where the self-assembled vascular network anastomosed with the 3D bioprinted endothelium, we observed the presence of erythrocytes inside capillaries with 15–25 µm in diameter (Figure 7D). By dynamically monitoring RBC, we discovered that they were able to flow through the capillaries with an average velocity of 0.1 mm^{-1} s (Figure 7E). This value lies within the range of experimental data reported in the literature for various solid malignancies in vivo, specifically in the range of 0.0001–0.17 mm^{-1} s,[46,47] thus corroborating the proper vascular functionality of our model.

2.7. Cancer Cell Migration, Invasion, and Metastasis

Treatment-resistant metastatic disease accounts for the majority of deaths in cancer patients. Metastasis is a complex, multistage biological process that includes cancer cell migration, extravasation out of the blood vessels, survival, and proliferation. Therefore, a 3D model aiming to simulate the metastatic cascade must provide a realistic microenvironment with space for cancer

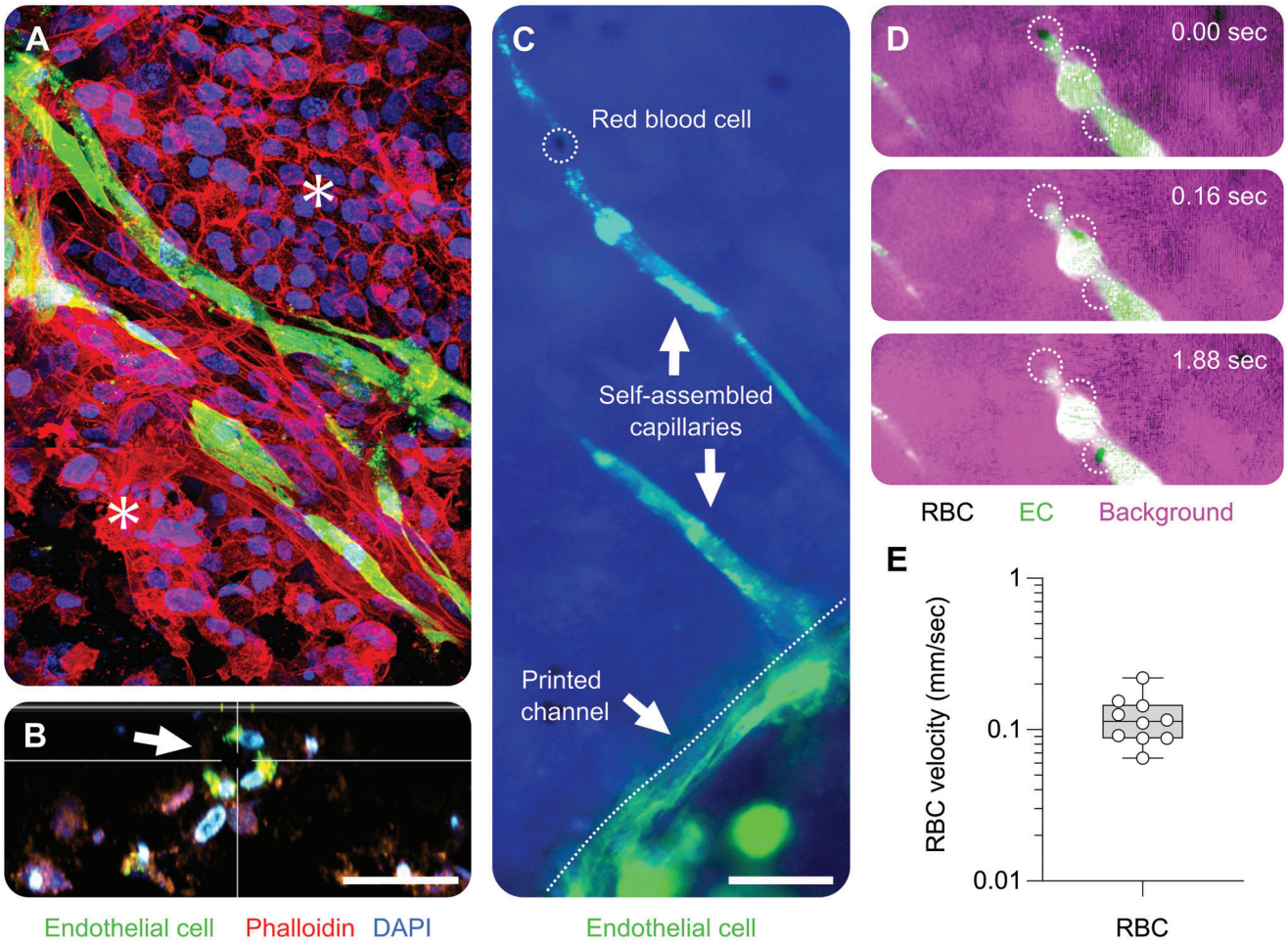

Figure 7. The self-organized vascular network surrounding the tumor spheroid is functional. A,B) Confocal (A) and 3D multiphoton (B) microscopy proves vascular sprouting into the tumor spheroid (indicated by the asterisks) and the formation of hollow structures (white arrow) after 21 d of dynamic cultivation. Scale bar in (A) and (B) = 25 µm). C) The capillary network's functionality was assessed by the circulation of red blood cells (RBC). An RBC (white dashed circle) inside a newly formed vessel is highlighted. The dotted line indicates the border between the printed channel and the matrix. Scale bar = 50 µm. D) Time-lapse images show the RBC motion by indicating three different positions (dashed circles) inside a 25 µm-wide capillary. E) The quantification of the velocity of RBC flowing inside the vascular structures is presented as box plot. Data are presented as mean velocity values expressed as mm^{-1} s of $n = 10$ individual RBC.

cells to migrate, perfused vessels, and it must allow long term observation to let the process occur spontaneously.

In this study, we assessed the role of the self-evolved vascular network in cancer cell migration by incorporating tumor spheroids into bioreactors with either both EC and fibroblasts or only fibroblasts in the surrounding hydrogel matrix. The tumor spheroid was strategically positioned at a distance of 500–800 µm from the bioprinted endothelium, thereby excluding any direct perturbations of fluid flow on the spheroid. After 7 d of dynamic cultivation, large-field confocal images showed the tumor spheroid still distant from the bioprinted endothelium (**Figure 8**A). In contrast, confocal images taken after 21 d revealed a significant change: cancer cells had bridged the space that initially separated the tumor spheroid from the vascular supply, infiltrating both the self-assembled vascular network and the bioprinted endothelium (Figure 8B–D). We investigated the presence of migrating and potentially metastatic cancer cells in media collected from bioreactors over 7, 14, and 21 d of dynamic cultivation. In the absence of EC in the matrix surrounding the tumor spheroid, no cancer cells were found in the culture media at day 7, with only a few appearing by day 14. In contrast, when EC were present in the matrix, cancer cells were detectable in the culture medium as early as day 7, and their number increased 11-fold by day 14 and 17-fold by day 21 (Figure 8E). By day 21 of dynamic cultivation, we calculated a release of ≈200 cancer cells per bioreactor into the circulating medium, a number significantly higher than that observed in the absence of EC surrounding the tumor spheroid (Figure 8E).

Taken together, these results underscore that a functional, self-assembled vascular network capable of forming connections with the bioprinted endothelium (as shown in Figure 7) not only allows for the flow of RBC and beads, but also for the spontaneous migration of cancer cells from the initial tumor cell mass into the circulation. Thus, beyond the novelty of an autonomously grown vasculature, the development of a model with the spatial and temporal ability to mimic the onset of cancer cell metastasis

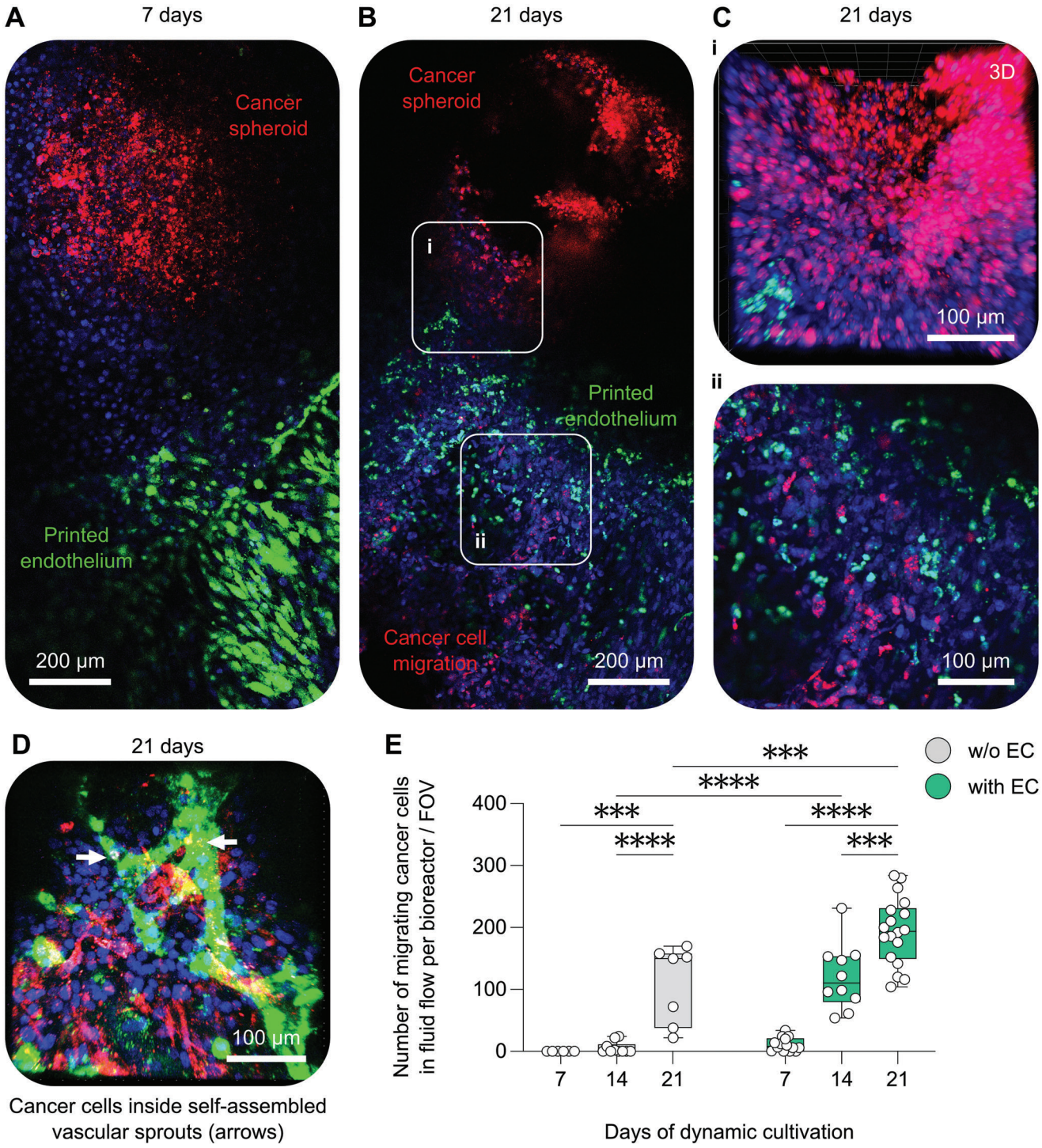

Figure 8. Presence of a vascular network surrounding tumor spheroids enables dissemination of cancer cells into circulating medium. A) Confocal microscopy image shows the separation between the tumor spheroid (DiD-labeled A431 cancer cells; in red) and the bioprinted endothelium (GFP-expressing HUVEC; in green) at 7 d of dynamic cultivation. B–D) At 21 d of dynamic cultivation, cancer cells have infiltrated deep in the ECM (B, C-i), and were found both in the bioprinted endothelium (B, C-ii), and inside the self-assembled capillaries (D). E) The number of DiD-labeled cancer cells found in fluid flow increased over time of dynamic cultivation, and was significantly higher when both EC and fibroblasts (vs fibroblasts alone) were present in the surrounding of the tumor spheroid. Data are displayed as mean ± SD of $n = 8$–18 technical replicates, acquired from $n = 2$–6 bioreactors, across $n = 4$ independent experiments. Statistical significance was assessed by a two-way Anova followed by Tukey's test for multiple comparisons; $^{*}P < 0.05$, $^{**}P < 0.01$, $^{***}P < 0.001$, and $^{****}P < 0.0001$.

represents a significant advance in both materials science and the biological aspects of tumor modelling.

2.8. 3D Mesoscopic Tumors Resemble Stromal and Vascular Features of Patient-Derived Xenograft Models in Mice

A crucial aspect in the development of physiologically relevant models of human malignancies in vitro, is the capacity to reproduce key features of the disease in vivo, including specific phenotypic and molecular signatures. For validating the translational potential of our approach, we set to use it for the cultivation of patient-derived material. We utilized previously established cell lines enriched with breast cancer stem cells (BCSC).[48–50] These were isolated from individual patient tumors subjected to neoadjuvant chemotherapy and classified as triple-negative breast cancer.[48] BCSC are promising targets for the development of novel anticancer therapies, as they are considered to be responsible for both cancer metastasis and therapy resistance.[51] Previous data revealed BCSC to be highly tumorigenic in mice, where they form tumors that recapitulate the architecture of the original patient material.[48,50]

We selected two BCSC cell lines, which were isolated from two TNBC patients, namely BCSC1 and BCSC2. These cell lines demonstrated distinct characteristics in both their original patient specimens and upon engraftment in mice. The tumors harvested from mice engrafted with BCSC1 appeared as round and pale masses, which is indicative of poor tumor vascularization. In contrast, the tumors from mice engrafted with BCSC2 appeared significantly red and hemorrhagic (**Figure 9**A). On histological analysis via Picrosirius red staining, BCSC1 displayed abundant collagen deposition around and within the tumor parenchyma (Figure 9A). CD31 staining revealed the presence of few vessels, mostly collapsed or squeezed between BCSC1 cancer cell sheets (Figure 9A). The histological analysis of BCSC2 specimens showed hemorrhagic necrosis on H&E staining, and collagen fibers surrounding the tumor lesion, forming a peripheral fibrotic rim, but they did not display strong infiltration into the tumor (Figure 9A). With respect to vascularization, CD31 staining revealed numerous blood vessels with open lumens (Figure 9A). Quantification confirmed the visual observation, revealing mean values of collagen area fraction % of 5.6 for BSCS1 and 1.7 for BCSC2 (p-value = 0.055), and mean values of CD31 area fraction % of 1 for BCSC1 and 2.8 for BCSC2 (p-value = 0.057) (Figure 9C).

BCSC isolation and 2D-culture were performed under defined conditions, including serum-free culture medium, Rho-kinase inhibitor, 2% Matrigel, and low oxygen environment. Therefore, although Matrigel has limitations, identical conditions were applied for the 3D cultivation of BCSC spheroids, which were embedded with stromal cells and EC in a serum-free fibrin-collagen hydrogel mix containing 2% Matrigel upon reaching mean sizes of 300 µm. Shifting from a Matrigel-containing environment to a Matrigel-free one could potentially induce alterations in BCSC growth rate and phenotype, which we wanted to avoid in order to maintain the physiological features of our model. Nevertheless, we wish to highlight that our use of Matrigel was limited to 2% in our hydrogel mix. This represents a significant improvement over previous studies involving BCSC, which solely relied on pure Matrigel for 3D cultivation of BCSC spheroid.[52]

During 3D cultivation, both BCSC1 and BCSC2 increased in size and interacted with their environment (Figure 9B). BCSC1 (red) demonstrated preferential interaction with fibroblasts (blue), which progressively surrounded and infiltrated the tumor spheroid, resulting in magenta color on merged images indicative of colocalization between cancer cells and fibroblasts (Figure 9B,D; Figure S6, Supporting Information). Interestingly, between six and nine days of 3D cultivation, migration of single cancer cells and finger-like projections were visible (Figure 9B). To further validate this observation, fluorescence-labeled cancer cells were identified in the media collected from bioreactors where BCSC1 spheroids were cultivated (Figure S6, Supporting Information). Conversely, akin to observations made in murine histological specimens, BCSC2 were strongly vascularized, showing interactions between cancer cells and EC (Figure 9B). This interaction promoted EC sprouting into the tumor spheroids (Figure 9B,E). However, BCSC2 grew much slower and did not show the invasive phenotype of BCSC1. In line with this, only BCSC1 were detected in the culture medium (Figure S6C, Supporting Information).

Additional comparative analysis of gene expression profiles of key markers involved in angiogenesis (e.g., VEGFR2, PECAM-1, Ang2) and ECM production/remodeling (e.g., Collagen 1, Collagen 6, fibronectin, MMP2, MMP9) confirmed the more angiogenic features of BCSC2 as compared to BCSC1, as evidenced by the statistically significant increased expression of, e.g., VEGFR2 and Ang2 (**Figure 10**A).

For the BCSC1 model, mouse xenograft tumor tissue was available for comparison (note that the mouse xenografts are genetically similar to the original patient tumor,[48] which is discussed later). The gene expression pattern of BCSC1, cultivated in our bioreactors, was more similar to mouse xenografts than that of regular spheroids (Figure 10B). These data indicate that our bioengineering approach is suitable for the cultivation of patient-derived material and that it has the potential to capture the phenotypic heterogeneity of human malignancies, similar to in vivo engraftment of cancer cells in mice.

3. Discussion

There is great interest in finding alternatives for animal experimentation. Advancements in microfabrication and microfluidics have contributed to the creation of vascularized multicellular models and the emergence of human-relevant preclinical models.[53,54] The most common approaches either comprise PDMS microfluidic chips or 3D bioprinting to form vascular like-structures.

Every approach has unique advantages and challenges. Microfluidic chips, for instance, allow high throughput at relatively low material costs.[53] The single-plane arrangement of cells also simplifies the visualization of cell–cell interactions.[13] In microfluidic chips, the formation of a functional vasculature is achieved by merging the inherent ability of EC to form capillary networks in 3D matrices with a specific chip design. This design includes microposts positioned at a distance of ≈100 µm apart that delineate the media from the cell-hydrogel and create entry points to the vasculature.[15] However, this design

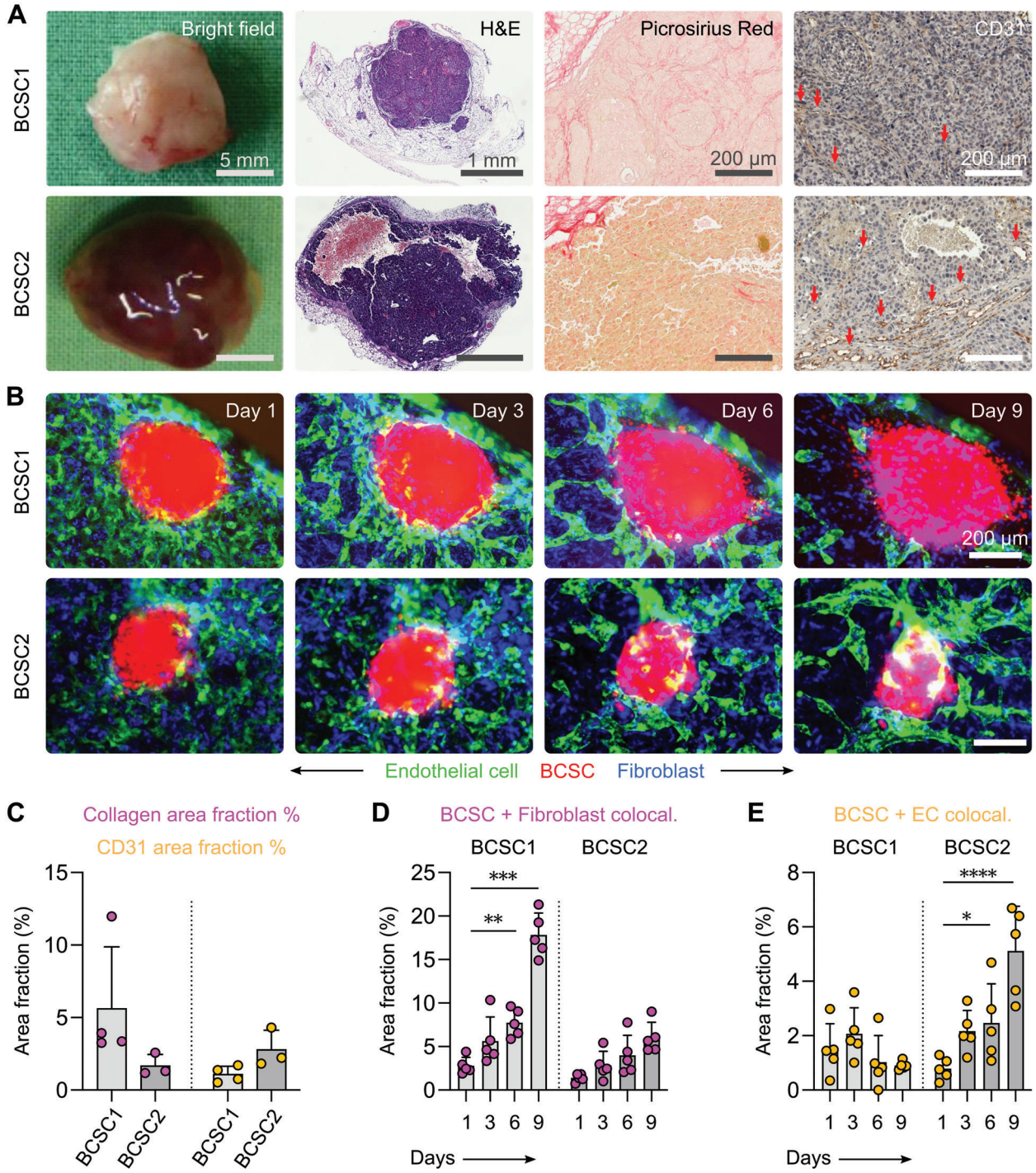

Figure 9. The 3D mesoscopic artificial tumors mimic stromal and vascular features of patient-derived xenografts in mice. A) Bright field images of harvested BCSC1 and 2 tumors, histological analysis of collagen I and III deposition (Picrosirius Red staining) and blood vessels (CD31 staining) exemplified the phenotypic differences between two patient-derived triple-negative breast cancer stem cell xenografts, i.e., the poorly vascularized and fibrotic BCSC1, and the highly vascularized BCSC2. B) Homo-spheroids of BCSC1 and BCSC2 were embedded in the ECM-mimicking hydrogel along with fibroblasts and EC. Upon 3D dynamic cultivation, BCSC1 displayed higher interaction with fibroblasts (blue) over EC (green), whereas BCSC2 showed strong interaction with the surrounding vascular network, which progressively infiltrated the tumor spheroid. C) Quantification of Picrosirius Red and CD31 staining on murine histological specimens confirmed higher desmoplasia (i.e., collagen content) in BCSC1 tumors and higher vascularization (i.e., CD31 area fraction) in BCSC2 tumors. D) Colocalization analysis (computing of magenta area fraction) between fibroblasts (blue) and BCSC spheroids (red) indicated higher values for BCSC1 as compared to BCSC2. E) Colocalization analysis (computing of yellow area fraction) between endothelial cells (green) and BCSC spheroids (red) confirmed higher values for BCSC2 as compared to BCSC1. Data are displayed as means ± SD of $n = 3$–4 biological replicates in (C), $n = 5$ replicates in (D). E) Statistical significance was assessed by a two-way Anova followed by Tukey's test for multiple comparisons. $^{*}P < 0.05$, $^{**}P < 0.01$, $^{***}P < 0.001$, and $^{****}P < 0.0001$.

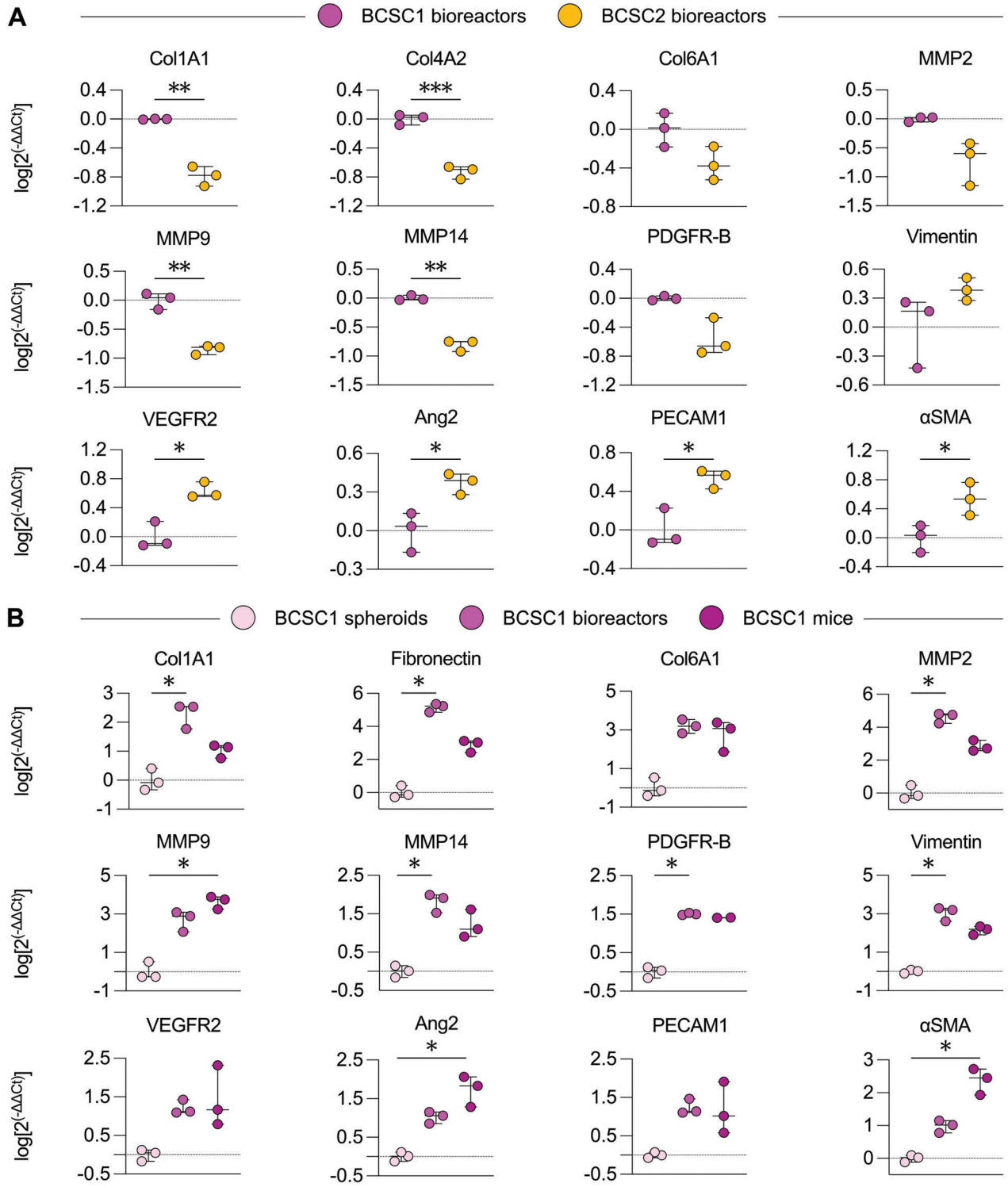

Figure 10. Fibrogenic and angiogenic gene expression. A) Quantitative real-time PCR (qPCR) was applied to compare the expression levels of genes involved in angiogenesis, ECM deposition, and remodeling between BCSC1 and BCSC2. The selected target genes were normalized to the expression of the housekeeping gene Glyceraldehyde 3-phosphate dehydrogenase (GAPDH), to ensure consistency across samples. The results revealed a statistically significant lower expression of collagen 1, collagen 4, MMP9, MMP14 in BCSC2 as compared to BCSC1, and a significantly higher expression of angiogenesis-related markers, including VEGFR2, ANG2, PECAM1, and αSMA. B) Gene expression analysis shows that BCSC1 spheroids cultivated in our bioreactors more closely resemble BCSC1 tumors grown in mice, compared to BCSC1 spheroids alone. Data are presented as relative fold change in gene expression of $n = 3$ replicates. Statistical significance was assessed via (A) an unpaired t test with Welch's corrections (A) and a Kruskal–Wallis test with Dunn's corrections for multiple comparisons in (B); $^{*}P < 0.05$, $^{**}P < 0.01$, $^{***}P < 0.001$, and $^{****}P < 0.0001$.

is somewhat artificial, as its functionality is more forced than naturally evolved. Furthermore, spatial restrictions in microfluidic chips, often characterized by an inner height of less than 500 μm, limit the growth of tumors to millimeter-sized scales, which are most relevant clinically.[13,20,21,23,55] Additionally, most microfluidic technologies have a limited lifespan, often just six days, restricting the observation time required for many relevant biological processes to spontaneously occur, such as metastasis. Although PDMS chips have been successfully employed to emulate discrete steps of the metastatic cascade in vitro, the methods often require introducing cancer cells as suspensions into the system via a lateral media port. By applying a hydrostatic pressure drop, the cells are forced into the vascular network, where they arrest and grow, establishing "micrometastases".[13,56–58] Alternatively, cells may be positioned on top of a microvascular network.[59] However, neither of these approaches really mimic the entire cascade of cancer cell activation (e.g., by hypoxia gradients and cytokines), migration, and interaction with and crossing of the endothelium.

Our methodology differs from conventional microfluidic approaches by combining bioprinting and bioengineering techniques to create a mesoscopic, physiological 3D tumor model. We bioprinted tumor feeding vessels with natural vessel conformation, including curves, anastomoses, and variations in lumen size. Bioprinting vascular channels with natural shapes addresses the relationship between vessel structure and internal hydrodynamic properties, which stimulate mechanotransduction in endothelial cells, thus affecting gene expression, cell adhesion, and the expression of angiogenesis-related factors.[17,60–62] Our PEEK bioreactor with optically transparent windows allowed real-time monitoring of cell growth, and its inner spaces of centimeter thickness could contain sufficient volumes of hydrogel for long-term durability while enabling growth of biological material beyond the micrometer scale. We utilized a high concentration of cells (10 million cells per ml of hydrogel blend) to mimic the cellularity and basic composition of tissues in vivo. The self-evolved vascular structure infiltrates the tumor spheroids, forms spontaneous and functional connections with the bioprinted endothelium, and proved perfusability to erythrocytes and 10 μm polystyrene μbeads. We dynamically monitored erythrocytes and beads, finding that their movement through self-assembled capillaries matched the flow velocities reported in literature for various in vivo solid malignancies.[46,47] The successful establishment of spontaneous and functional connections between the self-assembled vascular network and the bioprinted endothelium is a strength of this platform, opening perspectives for research on drug delivery and cell therapies. Furthermore, we observed cancer cells spontaneously departing from a tumor spheroid, invading into the self-assembled vascular network, and migrating through the bioprinted endothelium into the fluid flow. Our system marks a significant advance in the field by allowing the observation of the spontaneous transition of an in vitro tumor to a metastatic phenotype, up to the intravasation stage. In the future, this approach could potentially be extended to mimic the entire metastatic cascade by linking the artificial tumor model to, for example, a second bioreactor containing a tissue model that replicates a secondary site for cancer cell colonization.

Despite a lower throughput when compared to microfluidic chips, 3D bioprinting of vascular-like structures inside millimeter-sized devices, combined with other bioengineering strategies, including the use of matrices with prefabricated porosities, has expanded the scale and durability of vascularized tissue structures.[4,25,29,30] These approaches have shown promise for cultivating patient-derived material, particularly for high medical need diseases and inaccessible malignancies, such as glioblastoma. For example, 3D cultivation of patient-derived glioblastoma and stromal cells was successfully sustained by bioprinting of a vascular-like structure inside a customized PDMS chamber.[28] A high-density EC and pericyte cell suspension was injected into the hollow structure after removal of the sacrificial material. 2D-cultured cancer and stromal cells were resuspended in a hydrogel-based ECM substitute consisting of fibrin and gelatin. The functionality of the bioprinted vessel model was demonstrated by injecting high MW dextran, which was retained by an endothelium-like structure. Even though the process of tumor angiogenesis was not detailed in that study, cancer cells grown in the 3D platform displayed growth curves, drug responses, and gene expression patterns that were comparable to those of orthotopic cancer mouse models. Similarly, we successfully cultivated patient-derived material in our platform, recapitulating the heterogeneous interactions of cancer cells with their microenvironment. Tumors grown in our bioreactors not only better resembled genetic signatures of tumors engrafted in mice as compared to standard 3D tumor spheroids, but also captured the human malignancies' heterogeneity, thereby further substantiating the usefulness of our mesoscopic in vitro models.

The use of mesoscopic models has allowed for the cultivation of tumor spheroids in between vascular-like parallel channels for extended periods of up to 70 d.[63] Although the process of tumor vascularization was not reported, that method allowed for long-term assessment of tumor spheroid growth and therapy response using noninvasive high-resolution fluorescence molecular tomography. It is noteworthy that clinical imaging modalities (e.g., MRI) that can provide important noninvasive insights into tissue morphology, tumor volume, cellularity, metabolism, and vascular structure and function can only be applied in mesoscopic models, such as the chorioallantoic membrane (CAM) model.[64] Operating at the mesoscopic scale bridges a critical gap between microscale models, which often miss crucial multicellular interactions, and the macroscale of in vivo models, which are heterogeneous and strongly influenced by their environment and host. The mesoscopic in vitro models capture the best of both, the micro and macro scale: on the one hand, they enable a high degree of standardization and the possibility to systematically study the particular impact of added cells or drugs, and on the other hand the mimicking of a (patho-)physiological environment with pressure and oxygen gradients, spontaneous stroma formation, necrosis, tumor cell invasion, metastasis, and tumor sizes that are clinically representative.[4,65] The mesoscopic scale also offers sufficient space for cellular proliferation, organization, motility, and long-term observation to let these process occur spontaneously.

Overall, mesoscopic in vitro models, such as the one we propose, can potentially be used in the future to screen drug responses, test new therapeutic strategies (including immunotherapies that require complex cellular interactions), and obtain

information at the molecular level in a more physiological environment than traditional 2D cell cultures allows.

4. Conclusion

We established a platform where tumor spheroids embedded in ECM mimics can grow naturally to the mesoscopic scale and interact with the surrounding vascular network. Importantly, the capillary network infiltrates the spheroids and is functional, mirroring the complex and dynamic interactions between tumors and their microenvironment in vivo. In addition, the conversion of the spheroids to an invasive and metastatic tumor could be tracked the presence of migrating cancer cells in the circulating fluid was demonstrated. Finally, by utilizing a modular approach, we are able to cultivate patient-derived material and capture the phenotypic heterogeneity of human malignancies. This novel 3D platform has the potential to improve the predictive power of in vitro experimentation in basic cancer research and drug development, thus, contributing to the reduction of animal use.

5. Experimental Section

The bioreactors were modeled using Autodesk Inventor and made of PEEK using CNC milling. The bioreactors were functionalized with stainless steel Luer-lock adapters and connected to oxygen-permeable silicone tubing for dynamic cultivation. All components are autoclavable, biocompatible, chemically resistant, and were sterilized before assembly. The bioprinting process was performed in a sterile environment comprising a custom-made housing system equipped with sterile-filtered air and a cooling system. The vascular bioink used in the bioprinting process consisted of gelatin mixed with EC, which was extruded through a micro-extrusion bioprinter. A fibrinogen-collagen hydrogel blend was chosen as a mimic of the ECM and prepared as already described.[24,25,27] The ECM blend was used to harvest EC, stromal cells, and tumor spheroids, which were positioned inside the bioreactors in the space comprised by the bioprinted gelatin strands. After the hydrogel blend solidified, the bioreactor was incubated at 37 °C for the gelatin to liquefy and the EC to settle. Dynamic flow regimes were applied through the vascular network in a recirculating fluid loop. Bioreactors were cultivated for up to three weeks and longitudinally monitored using fluorescence microscopy. Perfusion of the system with erythrocytes or fluorescent polystyrene microbeads was used to test the network's functionality. All data are presented as mean ± standard deviation (SD). The number of experimental replicates and statistical analyses are indicated in the figure legends. Further explanation on the materials and methods and the scientific conduct is presented in Figure 2 and in the Experimental Section (Supporting Information).

Supporting Information

Supporting Information is available from the Wiley Online Library or from the author.

Acknowledgements

The authors gratefully acknowledge financial support by the European Fund for Regional Development (F.D., T.L. – TAKTIRA: Project number: EFRE-0801767 and S.B., J.M. – TAKTIRA: Project number: EFRE-0801765), the European Research Council (T.L. – ERC Consolidator Grant 864121: Meta-Targeting), the German Research Foundation (T.L. – DFG: GRK2375 (Project number: 331065168), and the German Cancer Aid (F.D., A.M.S. – SDK Postgraduate Program MSSOABCD). Dr. Sanja Aveic, Roswitha Davtalab, and Rodrigo Salazar Ortiz, Department of Dental Materials and Biomaterial Research, RWTH Aachen University Hospital, Aachen, Germany, are thanked for isolating and providing mesenchymal stem cells and for technical support during the bioprinting procedures. Dr. Karolin Römhild, Department of Nanomedicine and Theranostics, Institute for Experimental Molecular Imaging, RWTH Aachen University Hospital, Germany, is thanked for isolating the red blood cells. Dr. Marcelo Szymanski de Toledo, Department of Hematology, Oncology, Hemostaseology and Stem Cell Transplantation, RWTH Aachen University Hospital, Aachen, Germany, is thanked for supporting with methods for the isolation of cells from hydrogels. This work was supported by the Core Facility "Two-Photon Imaging", by the Confocal Microscopy Facility, and by the Immunohistochemistry Facility, core facilities of the Interdisciplinary Center for Clinical Research (IZKF) Aachen within the Faculty of Medicine RWTH Aachen University.

Open access funding enabled and organized by Projekt DEAL.

Conflict of Interest

The authors declare no conflict of interest.

Author Contributions

F.D. and N.H. contributed equally to this work. F.D., B.T., H.F., T.L., and F.K. conceptualized the study. F.D., N.H., J.S., B.T., A.M.S., H.F., and F.K. designed the experiments. B.T., T.L., H.F., and F.K. supervised the study. N.H., J.S., and H.F. designed the bioreactors, the printing procedures, and performed the printing of the vascular-like structures. N.H. performed the structural modeling of the bioprinted gelatin strands. R.N. performed the numerical modeling and fluid mechanics simulation. F.D. and A.M.S. performed the high-resolution CT imaging of bioprinted structures. F.D., B.T., and R.D. performed the cell culture. F.D. and R.D. performed 3D cell culture. S.B. performed cell culture of patient-derived breast cancer stem cells and formation of 3D tumor spheroids. F.D., N.H., and B.T. performed the casting and dynamic cultivation of the vascularized tumors. F.D. and A.M.S. calculated the RBC and beads velocity. F.D. and A.M.S. processed the samples for flow cytometry, PCR analysis, and human cytokine antibody array. A.M.S. and J.B. performed flow cytometry. F.D. and R.D. performed the human cytokine antibody array and RD performed the PCR experiments. F.D., B.T., and A.M. performed fluorescence microscopy and histology. M.V. performed multiphoton imaging. G.M.N. performed the confocal imaging. S.B. and J.M. provided tissue specimens of patient-derived cancer cells engrafted in mice. S.vS. provided human surgical specimens of skin squamous cell carcinoma. F.D. and N.H. wrote the original manuscript. F.D., N.H., and A.M.S. designed the figures. F.D. . and A.M.S. analyzed the data and performed statistical analyses. All authors contributed to the revision of the manuscript.

Data Availability Statement

The data that support the findings of this study are available from the corresponding author upon reasonable request.

Keywords

3D bioprinting, 3D multicellular tumor spheroid, bioengineering, hydrogels, metastasis

Received: April 5, 2023
Revised: August 5, 2023
Published online: October 22, 2023

[1] J. Zurlo, D. Rudacille, A. M. Goldberg, *Environ. Health Perspect.* **1996**, *104*, 878.
[2] M. Björnmalm, K. J. Thurecht, M. Michael, A. M. Scott, F. Caruso, *ACS Nano* **2017**, *11*, 9594.
[3] C. K. Osborne, K. Hobbs, G. M. Clark, *Cancer Res.* **1985**, *45*, 584.
[4] K. M. Yamada, E. Cukierman, *Cell* **2007**, *130* , 601.
[5] J. M. Lee, P. Mhawech-Fauceglia, N. Lee, L. C. Parsanian, Y. G. Lin, S. A. Gayther, K. Lawrenson, *Lab. Investig.* **2013**, *93*, 528.
[6] P. A. Kenny, G. Y. Lee, C. A. Myers, R. M. Neve, J. R. Semeiks, P. T. Spellman, K. Lorenz, E. H. Lee, M. H. Barcellos-Hoff, O. W. Petersen, J. W. Gray, M. J. Bissell, *Mol. Oncol.* **2007**, *1*, 84.
[7] S. P. Carey, A. Starchenko, A. L. Mcgregor, C. A. Reinhart-King, *Clin. Exp. Metastasis* **2014**, *30*, 615.
[8] A. J. Rice, E. Cortes, D. Lachowski, B. C. H. Cheung, S. A. Karim, J. P. Morton, A. Del Río Hernández, *Oncogenesis* **2017**, *6*, e352.
[9] Y. Matsumura, H. Maeda, *Cancer Res.* **1986**, *46*, 6387.
[10] S. N. Bhatia, D. E. Ingber, *Nat. Biotechnol.* **2014**, *32* , 760.
[11] K. Ronaldson-Bouchard, G. Vunjak-Novakovic, *Cell Stem Cell* **2018**, *22*, 310.
[12] J. A. Whisler, M. B. Chen, R. D. Kamm, *Tissue Eng., Part C* **2014**, *20*, 543.
[13] M. B. Chen, J. A. Whisler, J. Fröse, C. Yu, Y. Shin, R. D. Kamm, *Nat. Protoc.* **2017**, *12*, 865.
[14] J. Kim, M. Chung, S. Kim, D. H. Jo, J. H. Kim, N. L. Jeon, *PLoS One* **2015**, *10*, 0133880.
[15] S. Kim, H. Lee, M. Chung, N. L. Jeon, *Lab Chip* **2013**, *13*, 1489.
[16] S. Kim, M. Chung, J. Ahn, S. Lee, N. L. Jeon, *Lab Chip* **2016**, *16*, 4189.
[17] P. A. Galie, D.-H. T. Nguyen, C. K. Choi, D. M. Cohen, P. A. Janmey, C. S. Chen, *Proc. Natl., Acad. Sci. USA* **2014**, *111*, 7968.
[18] A. Sobrino, D. T. T. Phan, R. Datta, X. Wang, S. J. Hachey, M. Romero-López, E. Gratton, A. P. Lee, S. C. George, C. C. W. Hughes, *Sci. Rep.* **2016**, *6*, 31589.
[19] S. J. Hachey, S. Movsesyan, Q. H. Nguyen, G. Burton-Sojo, A. Tankazyan, J. Wu, T. Hoang, D. Zhao, S. Wang, M. M. Hatch, E. Celaya, S. Gomez, G. T. Chen, R. T. Davis, K. Nee, N. Pervolarakis, D. A. Lawson, K. Kessenbrock, A. P. Lee, J. Lowengrub, M. L. Waterman, C. C. W. Hughes, *Lab Chip* **2021**, *21*, 1333.
[20] Y. Nashimoto, R. Okada, S. Hanada, Y. Arima, K. Nishiyama, T. Miura, R. Yokokawa, *Biomaterials* **2020**, 229, 119547.
[21] K. Haase, G. S. Offeddu, M. R. Gillrie, R. D. Kamm, *Adv. Funct. Mater.* **2020**, *30*, 2002444.
[22] G. Bergers, L. E. Benjamin, *Nat. Rev. Cancer* **2003**, *3*, 401.
[23] Y. Nashimoto, T. Hayashi, I. Kunita, A. Nakamasu, Y.-S. Torisawa, M. Nakayama, H. Takigawa-Imamura, H. Kotera, K. Nishiyama, T. Miura, R. Yokokawa, *Integr. Biol.* **2017**, *9*, 506.
[24] D. B. Kolesky, R. L. Truby, A. S. Gladman, T. A. Busbee, K. A. Homan, J. A. Lewis, *Adv. Mater.* **2014**, *26*, 3124.
[25] D. B. Kolesky, K. A. Homan, M. A. Skylar-Scott, J. A. Lewis, *Proc. Natl. Acad. Sci. USA* **2016**, *113*, 3179.
[26] M. A. Skylar-Scott, S. G. M. Uzel, L. L. Nam, J. H. Ahrens, R. L. Truby, S. Damaraju, J. A. Lewis, *Sci. Adv.* **2019**, *5*, eaaw2459.
[27] J. Schöneberg, F. De Lorenzi, B. Theek, A. Blaeser, D. Rommel, A. J. C. Kuehne, F. Kiessling, H. Fischer, *Sci. Rep.* **2018**, *8*, 10430.
[28] L. Neufeld, E. Yeini, N. Reisman, Y. Shtilerman, D. Ben-Shushan, S. Pozzi, A. Madi, G. Tiram, A. Eldar-Boock, S. Ferber, R. Grossman, Z. Ram, R. Satchi-Fainaro, *Sci. Adv.* **2021**, *7*, eabi9119.
[29] A. A. Szklanny, M. Machour, I. Redenski, V. Chochola, I. Goldfracht, B. Kaplan, M. Epshtein, H. S. Yameen, U. Merdler, A. Feinberg, D. Seliktar, N. Korin, J. Jaroš, S. Levenberg, *Adv. Mater.* **2021**, *33*, 2102661.
[30] L. Debbi, B. Zohar, M. Shuhmaher, Y. Shandalov, I. Goldfracht, S. Levenberg, *Biomaterials* **2022**, *280*, 121286.
[31] T. Tariverdian, T. Navaei, P. B. Milan, A. Samadikuchaksaraei, M. Mozafari, *Adv. Funct. Polym. Biomed. Appl.* **2019**, *16*, 323.
[32] T. Kobayashi, H. J. Kim, X. Liu, H. Sugiura, T. Kohyama, Q. Fang, et al., *Am. J. Physiol.: Lung Cell Mol. Physiol.* **2014**, *306*, L1006.
[33] E. A. Aisenbrey, W. L. Murphy, *Nat. Rev. Mater.* **2020**, *5*, 539.
[34] N. J. Kaiser, R. J. Kant, A. J. Minor, K. L. K. Coulombe, *ACS Biomater. Sci. Eng.* **2019**, *5*, 887.
[35] T. Coradin, K. Wang, T. Law, L. Trichet, *Gels* **2020**, *6*, 36.
[36] M. Wachendörfer, E. M. Buhl, M. G. Ben, W. Richtering, H. Fischer, *Adv. Healthcare Mater.* **2023**, *10*, 2203302.
[37] E. Cholewinski, M. Dietrich, T. C. Flanagan, T. Schmitz-Rode, S. Jockenhoevel, *Tissue Eng., Part A* **2009**, *15*, 3645.
[38] J. Ehling, B. Theek, F. Gremse, S. Baetke, D. Möckel, J. Maynard, S.-A. Ricketts, H. Grüll, M. Neeman, R. Knuechel, W. Lederle, F. Kiessling, T. Lammers, *Am. J. Pathol.* **2014**, *184*, 431.
[39] E. Zudaire, L. Gambardella, C. Kurcz, S. Vermeren, *PLoS One* **2011**, *6*, 27385.
[40] H. Kang, K. J. Bayless, R. Kaunas, *Am. J. Physiol. Heart Circ. Physiol.* **2008**, *295*, H2087.
[41] J. W. Song, L. L. Munn, *Proc. Natl. Acad. Sci. USA* **2011**, *108*, 15342.
[42] C. M. Ghajar, X. Chen, J. W. Harris, V. Suresh, C. C. W. Hughes, N. L. Jeon, A. J. Putnam, S. C. George, *Biophys. J.* **2008**, *94*, 1930.
[43] K. Fujimoto, S. Erickson, M. Nakayama, H. Ihara, K. Sugihara, Y. Nashimoto, K. Nishiyama, T. Miura, R. Yokokawa, *Lab Chip* **2022**, *23*, 306.
[44] V. K. Lee, A. M. Lanzi, H. Ngo, S.-S. Yoo, P. A. Vincent, G. Dai, *Cell Mol. Bioeng.* **2014**, *7*, 460.
[45] I. S. Kinstlinger, G. A. Calderon, M. K. Royse, A. K. Means, B. Grigoryan, J. S. Miller, *Nat. Protoc.* **2021**, *16*, 3089.
[46] J. Munson, A. Shieh, *Cancer Manage. Res.* **2014**, *6*, 317.
[47] S. Walker-Samuel, T. A. Roberts, R. Ramasawmy, J. S. Burrell, S. P. Johnson, B. M. Siow, S. Richardson, M. R. Gonçalves, D. Pendse, S. P. Robinson, R. B. Pedley, M. F. Lythgoe, *Cancer Res.* **2018**, *78*, 1859.
[48] E. Metzger, S. S. Stepputtis, J. Strietz, B.-T. Preca, S. Urban, D. Willmann, A. Allen, F. Zenk, N. Iovino, P. Bronsert, A. Proske, M. Follo, M. Boerries, E. Stickeler, J. Xu, M. B. Wallace, J. A. Stafford, T. Kanouni, J. Maurer, R. Schüle, *Cancer Res.* **2017**, *77*, 5900.
[49] X. Li, J. Strietz, A. Bleilevens, E. Stickeler, J. Maurer, *Int. J. Mol. Sci.* **2020**, *21*, 404.
[50] J. Strietz, S. S. Stepputtis, M. Follo, P. Bronsert, E. Stickeler, J. Maurer, *Int. J. Mol. Sci.* **2021**, *22*, 1808.
[51] M. A. Velasco-Velázquez, V. M. Popov, M. P. Lisanti, R. G. Pestell, *Am. J. Pathol.* **2011**, *179*, 2.
[52] J. Dornhof, J. Kieninger, H. Muralidharan, J. Maurer, G. A. Urban, A. Weltin, *Lab Chip* **2022**, *22*, 225.
[53] D. E. Ingber, *Nat. Rev. Genet.* **2022**, *23*, 467.
[54] C. M. Leung, P. De Haan, K. Ronaldson-Bouchard, G.-A. Kim, J. Ko, H. S. Rho, Z. Chen, P. Habibovic, N. L. Jeon, S. Takayama, M. L. Shuler, G. Vunjak-Novakovic, O. Frey, E. Verpoorte, Y.-C. Toh, *Nat. Rev. Methods Primers* **2022**, *2*, 33.
[55] Y. Shin, S. Han, J. S. Jeon, K. Yamamoto, I. K. Zervantonakis, R. Sudo, R. D. Kamm, S. Chung, *Nat. Protoc.* **2012**, *7*, 1247.
[56] J. Song, A. Miermont, C. T. Lim, R. D. Kamm, *Sci. Rep.* **2018**, *8*, 179.

[57] J. S. Jeon, S. Bersini, M. Gilardi, G. Dubini, J. L. Charest, M. Moretti, R. D. Kamm, *Proc. Natl. Acad. Sci. USA* **2015**, *112*, 214.
[58] C. Hajal, L. Ibrahim, J. C. Serrano, G. S. Offeddu, R. D. Kamm, *Biomaterials* **2021**, *265*, 20470.
[59] L. I. Ibrahim, C. Hajal, G. S. Offeddu, M. R. Gillrie, R. D. Kamm, *Biomaterials* **2022**, *288*, 121728.
[60] S. Li, N. F. Huang, S. Hsu, *J. Cell. Biochem.* **2005**, *96*, 1110.
[61] T. A. Russo, A. M. M. Banuth, H. B. Nader, J. L. Dreyfuss, *PLoS One* **2020**, *15*, 0241040.
[62] N. G. Dela Paz, T. E. Walshe, L. L. Leach, M. Saint-Geniez, P. A. D'amore, *J. Cell Sci.* **2012**, *125*, 831.
[63] M. S. Ozturk, V. K. Lee, H. Zou, R. H. Friedel, X. Intes, G. Dai, *Sci. Adv.* **2020**, *6*, eaay7513.
[64] G. Winter, A. B. F. Koch, J. Löffler, F. Jelezko, M. Lindén, H. Li, A. Abaei, Z. Zuo, A. J. Beer, V. Rasche, *Front. Phys.* **2020**, *8*, 151.
[65] K. A. Homan, N. Gupta, K. T. Kroll, D. B. Kolesky, M. Skylar-Scott, T. Miyoshi, D. Mau, M. T. Valerius, T. Ferrante, J. V. Bonventre, J. A. Lewis, J. R. Morizane, *Nat. Methods* **2019**, *16*, 255.